Abstract

STOKELY, MATTHEW H.   Advanced Thermosyphon Targets for Production of the ^{18}F Radionuclide. (Under the direction of Dr. J.M. Doster).

Single phase and boiling batch water targets are the most common designs for the cyclotron production of ^{18}F via the ^{18}O(p,n)^{18}F reaction. Thermosyphon targets have design and operating characteristics which enable higher power operation than conventional boiling targets of like size. Experiments and calculations were conducted in order to characterize the performance of a 1.3 cc tantalum [^{18}F]Target. The test target led to the development of a variety of computational techniques as well as experimental methods that will be used in future target design and optimization. Computational methods include several applications of Monte Carlo Radiation Transport as well as Finite Element Analysis. In addition, experimental thermal hydraulic and radiochemical analyses were performed.

Advanced Thermosyphon Targets for Production of the ^{18}F Radionuclide

by

Matthew H. Stokely

A thesis submitted to the Graduate Faculty of
North Carolina State University
in partial fulfillment of the
requirements for the Degree of
Master of Science

Nuclear Engineering

Raleigh, North Carolina
2007

Approved By:

_____ _____

Dr. J. M. Doster   Dr. M. Bourham
Chair of Advisory Committee

_____ _____

Dr. B. Wieland   Dr. G. Bida

_____

Dr. M. Shearer

Biography

Matthew Hughes Stokely was born October 28, 1980 to Joseph and Amelia Stokely. He attended primary and high school in the small, backwoods town of Chapel Hill, North Carolina. At 17 he moved to the big city and enrolled in classes at North Carolina State University. In 2003, he graduated with a degree in Electrical Engineering. After a short career as a riverboat captain in Tennessee, he returned to NCSU to pursue a graduate degree in Nuclear Engineering. Upon graduating in May 2007, he will continue towards his Ph.D.

Acknowledgements

Table of Contents

List of Figures

List of Tables

Chapter 1

Introduction

1.1 Background

Medical imaging techniques are designed to provide high quality, *in vivo* pictures of internal human anatomy, biochemical and/or physiological events. Many of these techniques capture geometrical information, while others record functional information. Positron Emission Tomography (PET) is an imaging technique that can capture metabolic activity within the body. This technique is particularly useful in the detection and staging of, at present, seven different cancers and Alzheimer's disease.

PET imaging utilizes radiopharmaceuticals labeled with positron emitting radioisotopes. The most widely used compound is 2-deoxy-2-[^{18}F]fluoro-D-glucose (^{18}FDG), which is a sugar labeled with the fluorine-18 $\left(^{18}_{9}\text{F}\right)$ isotope. After the patient is injected with this compound, the sugar travels throughout the body. Areas with high metabolic rates will, in turn, have elevated concentrations of fluorine-18 from the metabolically trapped radiopharmaceutical [10,15].

Fluorine-18 decays by positron emission with a half-life of 109.7 minutes. The positron has a range of only a few millimeters in tissue before it slows sufficiently to combine with an electron. The annihilation reaction results in a pair of 511 keV photons separated by 180°. Because of this behavior, the photons can be recorded using coincidence detectors, and a 3-dimensional functional image can be computed [10,15].

The ^{18}F radionuclide is predominantly produced using an accelerator via the ^{18}O(p,n)^{18}F reaction. The target consists of either liquid $H_2{}^{18}O$ or gaseous $^{18}O_2$ contained in a

1

vessel upon which high energy protons (>2.5 MeV) are incident. Minimally, the production capability of any given target system is a function of beam energy and current. Due to the relatively small cross section of the nuclear reaction, it takes many thousand incident protons to produce one ^{18}F radionuclide [5]. As a result, much heat is generated by the incident protons as they slow down in the target. The design and development of target systems with increased heat removal capabilities and subsequent operation at higher beam energies and/or currents is actively underway at other facilities [11]. There are many challenges presented by these target systems including, but not limited to, thermal hydraulic limitations, radiation transport uncertainties, dynamic instabilities, and chemical compatibility restrictions.

1.2 Purpose

The purpose of this study is to characterize a prototype thermosyphon target system and develop it for F-18 production use at sub-kilowatt power levels. One kilowatt is a typical power level for most PET accelerators, but cyclotrons with much higher capacities do exist. For example, the Siemens-CTI RDS-111 produces 11 MeV protons at beam currents up to 100 μA (1.1 kW) and the GE PeTTrace produces 16.5 MeV protons at 150 μA (2.4 kW).

The prototype, named TS5 (Figure 1-1), is a fifth generation target developed by Bruce Technologies, Inc. The TS5 has a smaller internal volume (~1.5cm^3) than previous TS targets [3,13,17], and contains a tantalum liner in the beam strike region. The characterization of the TS5 target includes computational and experimental data. Experimental data includes thermal hydraulic performance for a wide range of operating conditions in addition to radionuclide yields using both natural abundance and [O-18]enriched target water. The thermal hydraulic performance is compared to

2

computational models developed using the COMSOL software package [2], while the F-18 yields are computed using MCNPX [6] and SRIM [18]. Specific goals included:

- Locating regions of high thermal resistance in order to eliminate contributing features in future designs.

- Determining the partitioning of heat transfer between the boiling and condensing regions within the target.

- Identify ranges of stable and reliable operation.

The development of the target system for production use included the design and fabrication of a PC-based control and data acquisition system. Design criteria included:

- Reliable manual or automated operation in all modes: fill, beam on target, delivery, and rinse.

- Display and record temperature, pressure, and beam current signals from instruments in the cyclotron vault.

- Provide safety interlocks to protect the target and cyclotron from undesirable regions of operation.

All experimentation and system development was performed at the Duke University PET facility where a CS-30 cyclotron is used routinely for the production of a variety of radiopharmaceuticals. This allowed for testing in a production environment as well as the use of specialized equipment not available in other venues.

The TS5 target proved to be inadequate with respect to fluoride production. However, the target provided a wealth of information which will be used to influence the design of future systems. In the course of characterizing TS5, a great deal of information concerning the physics of boiling water targets was revealed. Perhaps even more importantly, an analysis platform was developed which will be used to evaluate the performance of future target

systems. This analysis included experimental methods for collecting both thermal hydraulic and radiochemical performance data, as well as computational methods for simulation of fluid flow and heat transfer.
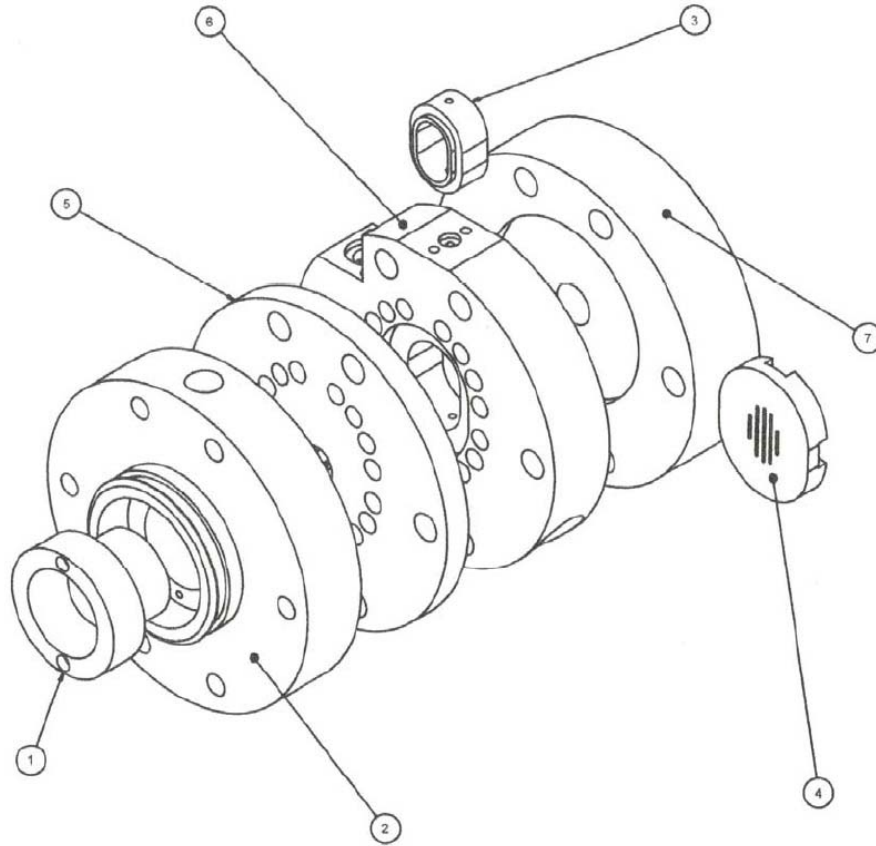
Figure 1-1: TS5 Exploded Parts Diagram (Humphrey 2006)

Table 1-1: TS5 Target Components

1	Graphite Sacrificial Grid
2	Front Cooling Manifold
3	Tantalum Chamber
4	Rear Window Support Grid
5	Front Window Support Flange
6	Target Center Flange
7	Rear Cooling Manifold

1.3 Related Work

Bruce Technologies, Inc. in collaboration with North Carolina State University, Bristol-Meyers Squibb Medical Imaging Division, and Wisconsin Medical Cyclotron, is currently developing a multi-kilowatt thermosyphon target and a >15 kilowatt recirculating target for large scale F-18 production. These target systems will likely be marketed to radiopharmaceutical distribution centers where higher yields are needed to supply [18]FDG over large distances.

The multi-kilowatt thermosyphon targets include the two models TS4.1 and TS4.2, designed for 10 mm and 15 mm proton beams [13]. These targets have relatively large internal volumes ($\sim$3cm^3) which are offset by their ability to tolerate more beam and, in turn, produce larger amounts of fluoride ion. These targets were designed primarily for proof of principle and were not intended for use in a regular production setting.

The recirculating target system utilizes a regenerative turbine pump to pass target water through the beam strike at high velocity [1,4,17]. The waste heat is then transferred from the target water through a compact heat exchanger to the cyclotron cooling system. The advantage of this design is the ability to run at very high power densities by suppressing boiling in the target medium.

GE Medical systems currently markets a high power boiling water target system with the PETTrace cyclotron, which has a normal operating thermal load of approximately 600W. The accelerator, however, has the capability to produce more than 150uA of beam at 16.5 MeV (2.4 kW), indicating the potential for target retrofitting.

Chapter 2

Target Design

2.1 Operating Principle

Single phase and conventional boiling batch target systems are the industry standard in [18]FDG PET production [12]. It is important to make the distinction, however, between a reflux type boiling water target and a thermosyphon target. Both types are designed to accommodate multi-phase heat transfer via evaporation and condensation. The difference between the two systems lies in the manner in which the chamber is pressurized (Figure 2-1).
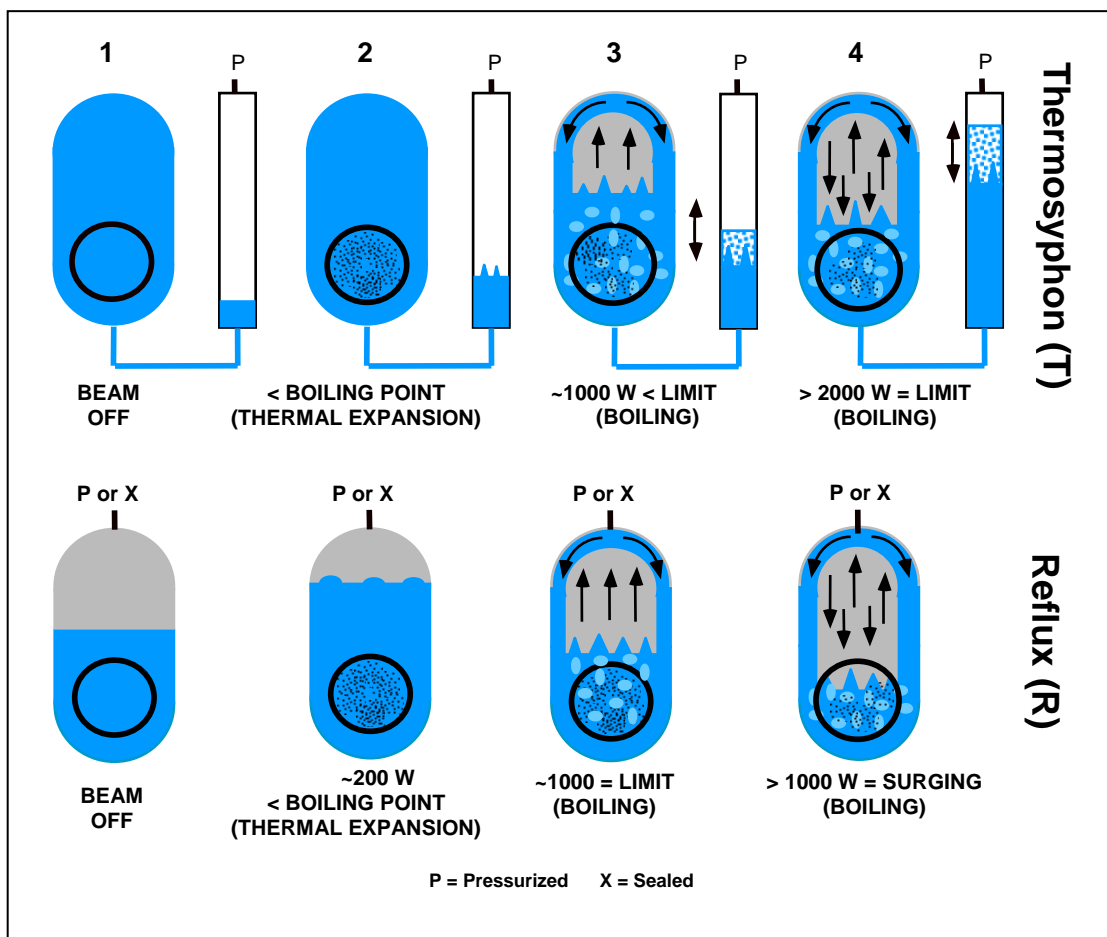
Figure 2-1: Qualitative Behavior of Reflux and Thermosyphon Targets

Reflux targets are pressurized from the top of the liquid volume. Because of this fact, there exists an initial amount of non-condensable gas which mixes with the liquid and vapor during bombardment. The non-condensable gas will impede condensation and lower the heat rejection capabilities of the target.

In contrast, a thermosyphon target is initially filled completely and pressurized from the bottom via an expansion volume or "standpipe". This maximizes the effective heat transfer area in the condensing region of the target volume by eliminating the presence of non-condensable gas. First principles calculations show that the presence of non-condensable gas reduces the heat transfer coefficient in a condensing film. Figure 2-2 shows the ratio of the wall heat flux with and without non-condensable gas for different wall temperatures and partial pressures. The ratio becomes very large as wall temperatures decrease. This is significant, as the condensing layer can become the limiting resistance to heat transfer as the target is cooled more aggressively.

2.2 Engineering Considerations

The TS5 target system has several features that make it unique. First and foremost is the composition of the beam strike region. Tantalum is a chemically inert material, which is extremely important in the reactive chemistry of the beam strike. However, its thermal conductivity is significantly lower than other candidate materials. Silver has been used extensively but introduces a small, yet significant, amount of contamination at high beam energies that can lead to poor [18]FDG synthesis. As a compromise between thermal and radio-chemical performance, the beam strike region contains a press-fit lining of tantalum in aluminum.
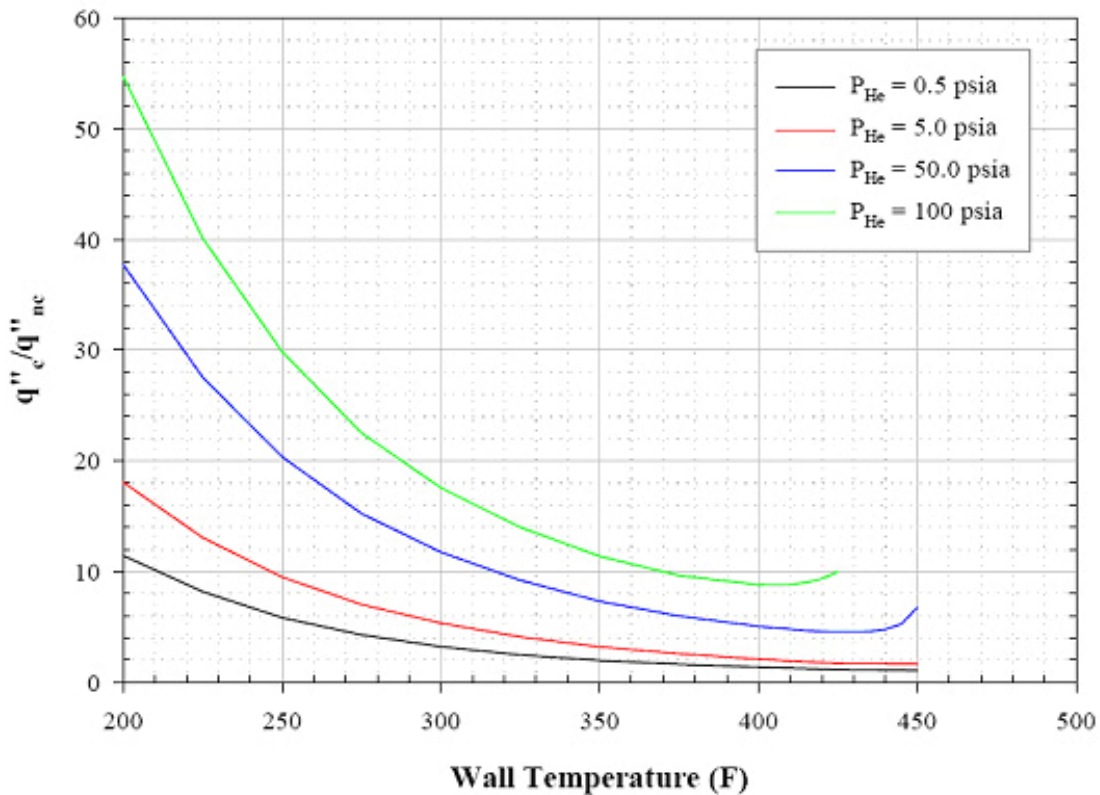
Figure 2-2: Effect of Non-Condensable Gas on Wall Heat Flux

In addition, the TS5 employs a modular construction. Any of the four flanges can be interchanged, allowing for geometry changes without redesigning the entire target. This could prove particularly useful, for example, in tailoring target volumes to match cyclotron beam energies in retrofitting applications.

Finally, the target system has an extremely versatile front window design. Both grid-supported and unsupported windows can be used depending on the application. For gathering experimental data such as yields or temperatures, it is useful to know the exact power input to the target water and an unsupported window is appropriate. For routine production,

however, the reliability and service life of the front window can be increased dramatically by using the support grid.

2.3 Design Modifications

Poor initial experimental yields indicated that the original TS5 may not have been range thick at 27 MeV. After eliminating other possible causes, for example beam misalignment, extending the beam strike depth was pursued. Simulating the coupled behavior of radiation transport and thermal hydraulics presents many mathematical and computational challenges which are beyond the scope of this study. In order to circumvent this issue, a void fraction of 0.3 was assumed in the beam strike region. This was assumed to be conservative since the total void fraction (α) in the target was not expected to exceed 0.2 (results since indicate that due to the high power densities in the beam even more void margin is necessary). The target was first modeled in MCNPX, a general purpose Monte Carlo radiation transport code that is capable of simulating both neutral and charged particle transport in arbitrary geometries. This calculation was performed by dividing the beam strike into 15 cylindrical slices arranged axially in series. A particle tally was performed on each slice in order to determine what target depth was necessary to stop all incident particles. It was found that 13 mm of depth was sufficient to stop no less than 97% of incident protons. Figures 2-3 and 2-4 contain the results from these calculations. SRIM, a less general Monte Carlo radiation transport code that calculates ranges and stopping powers for charged particles in one dimension, was also utilized. Figures 2-3 through 2-7 indicate that both computational methods are in agreement.

Beam Intensity vs Axial Position
400 psig Saturation Conditions, 26 MeV
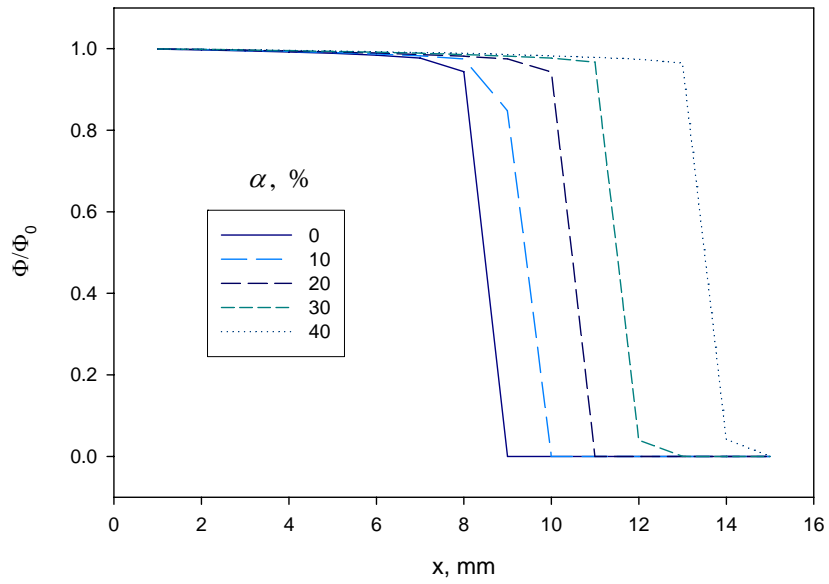
Figure 2-3: MCNPX Range Calculations to Determine Water Target Depth

Beam Intensity vs Axial Position
400 psig Saturation Conditions, 22 MeV
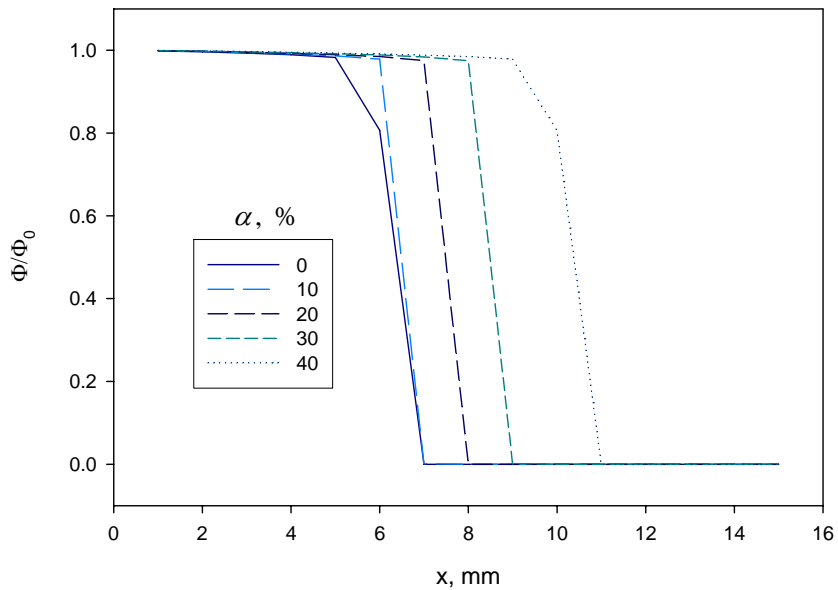
Figure 2-4: MCNPX Range Calculations to Determine Water Target Depth

Figure 2-5: Proton Range in Water vs. Void Fraction (Generated with SRIM 2006)
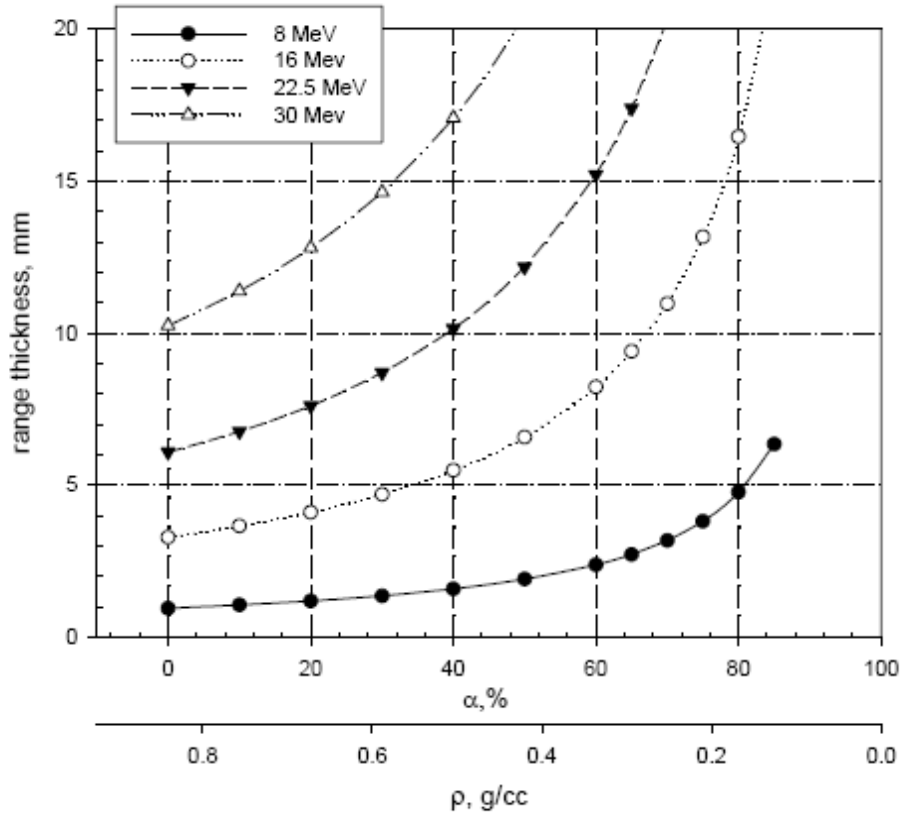
density, g/cc	% void	Energy, MeV	8	10	16	18	20	22.5	25	27.5	30
0.84768	0		0.95	1.42	3.29	4.07	4.92	6.09	7.37	8.75	10.25
0.762912	10		1.06	1.57	3.66	4.52	5.47	6.77	8.19	9.73	11.39
0.678144	20		1.19	1.77	4.11	5.09	6.15	7.61	9.21	10.94	12.81
0.593376	30		1.36	2.02	4.7	5.81	7.03	8.7	10.52	12.5	14.64
0.508608	40		1.59	2.36	5.49	6.78	8.2	10.15	12.28	14.59	17.08
0.42384	50		1.91	2.83	6.58	8.14	9.84	12.18	14.73	17.51	20.5
0.339072	60		2.38	3.54	8.23	10.17	12.3	15.22	18.41	21.88	25.62
0.296688	65		2.72	4.05	9.4	11.63	14.06	17.4	21.05	25.01	29.28
0.254304	70		3.18	4.72	10.97	13.57	16.41	20.3	24.56	29.18	34.16
0.21192	75		3.81	5.67	13.17	16.28	19.69	24.36	29.47	35.02	40.99
0.169536	80		4.77	7.09	16.46	20.35	24.61	30.45	36.84	43.78	51.25
0.127152	85		6.35	9.44	21.93	27.12	32.8	40.58	49.09	58.33	68.29

Minimum Target Thickness for Void Fraction (Density) Limit
400 psia Saturation Conditions
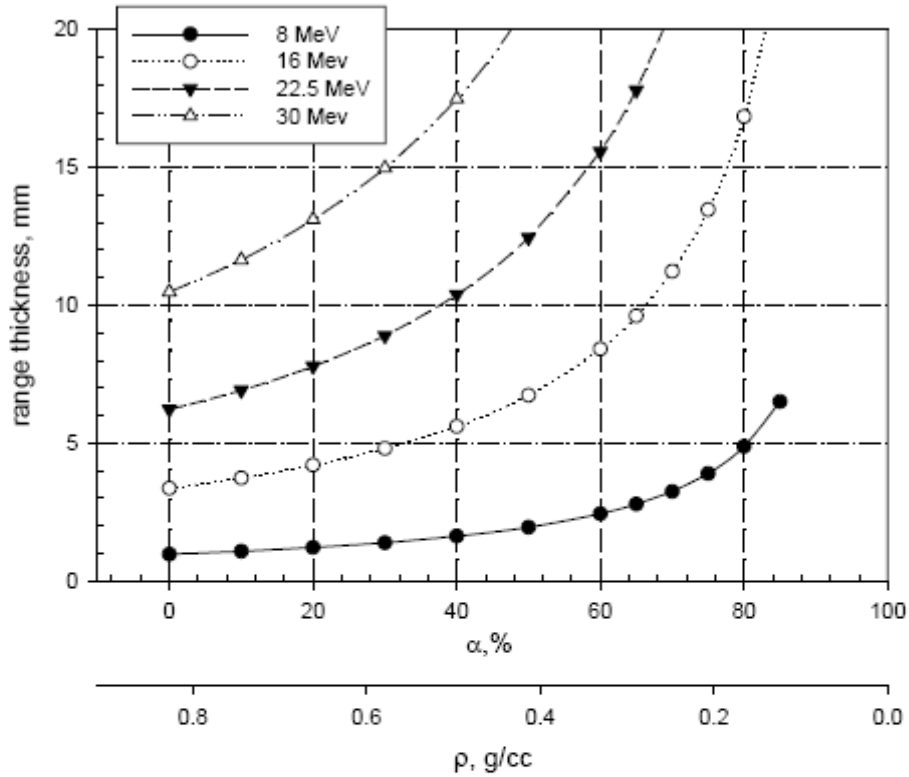
		Energy, MeV	8	10	16	18	20	22.5	25	27.5	30
density, g/cc	% void										
0.8282	0		0.98	1.45	3.37	4.17	5.04	6.23	7.54	8.96	10.49
0.74538	10		1.08	1.61	3.74	4.63	5.6	6.92	8.38	9.95	11.65
0.66256	20		1.22	1.81	4.21	5.21	6.3	7.79	9.42	11.2	13.11
0.57974	30		1.39	2.07	4.81	5.95	7.2	8.9	10.77	12.8	14.98
0.49692	40		1.63	2.42	5.61	6.94	8.4	10.39	12.57	14.93	17.48
0.4141	50		1.95	2.9	6.74	8.33	10.08	12.46	15.08	17.92	20.98
0.33128	60		2.44	3.63	8.42	10.41	12.59	15.58	18.85	22.4	26.22
0.28987	65		2.79	4.14	9.62	11.9	14.39	17.8	21.54	25.59	29.96
0.24846	70		3.25	4.83	11.23	13.88	16.79	20.77	25.13	29.86	34.95
0.20705	75		3.9	5.8	13.47	16.66	20.15	24.92	30.15	35.83	41.94
0.16564	80		4.88	7.25	16.85	20.83	25.19	31.17	37.71	44.81	52.45
0.12423	85		6.51	9.67	22.46	27.78	33.59	41.56	50.28	59.74	69.94

Figure 2-6: Proton Range in Water vs. Void Fraction (Generated with SRIM 2006)

Minimum Target Thickness for Void Fraction (Density) Limit
500 psia Saturation Conditions
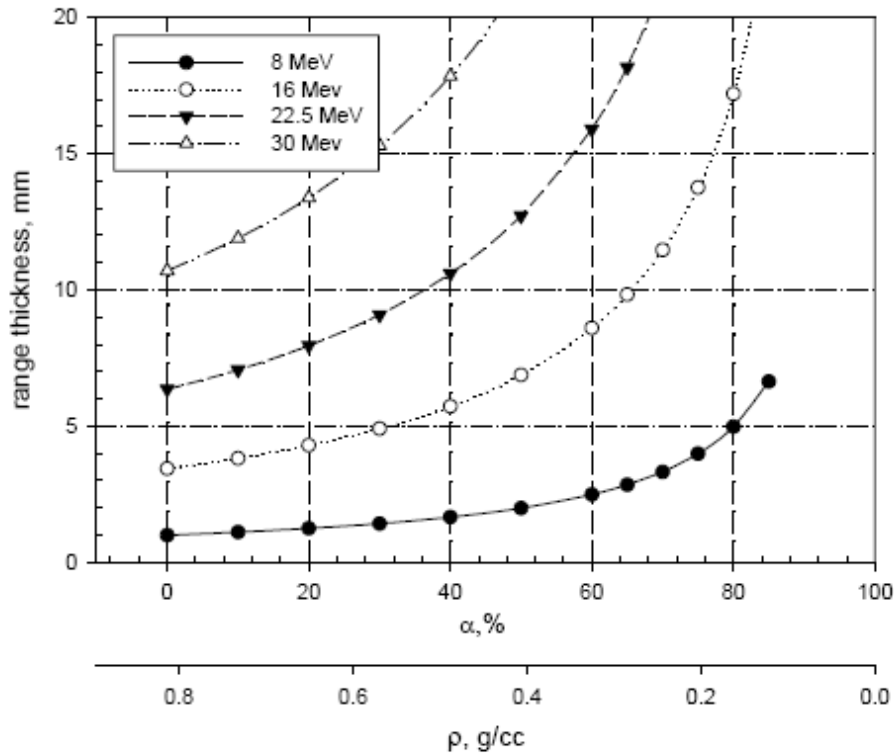
		Energy, MeV	8	10	16	18	20	22.5	25	27.5	30
density, g/cc	% void										
0.81098	0		1.00	1.48	3.44	4.25	5.14	6.36	7.70	9.15	10.71
0.729882	10		1.11	1.65	3.82	4.73	5.72	7.07	8.56	10.17	11.90
0.648784	20		1.25	1.85	4.30	5.32	6.43	7.96	9.62	11.44	13.39
0.567686	30		1.42	2.12	4.91	6.08	7.35	9.09	11.00	13.07	15.30
0.486588	40		1.66	3.42	5.73	7.09	8.57	10.61	12.83	15.25	17.85
0.40549	50		1.99	4.10	6.88	8.51	10.29	12.73	15.40	18.30	21.42
0.324392	60		2.49	5.13	8.60	10.63	12.86	15.91	19.25	22.87	26.78
0.283843	65		2.85	5.86	9.83	12.15	14.70	18.18	22.00	26.14	30.60
0.243294	70		3.32	6.84	11.47	14.18	17.15	21.21	25.67	30.50	35.70
0.202745	75		3.99	8.21	13.76	17.02	20.58	25.46	30.80	36.60	42.84
0.162196	80		4.98	10.26	17.20	21.27	25.72	31.82	38.50	45.75	53.55
0.121647	85		6.64	13.68	22.93	28.36	34.30	42.43	51.33	61.00	71.40

Figure 2-7: Proton Range in Water vs. Void Fraction (Generated with SRIM 2006)

13
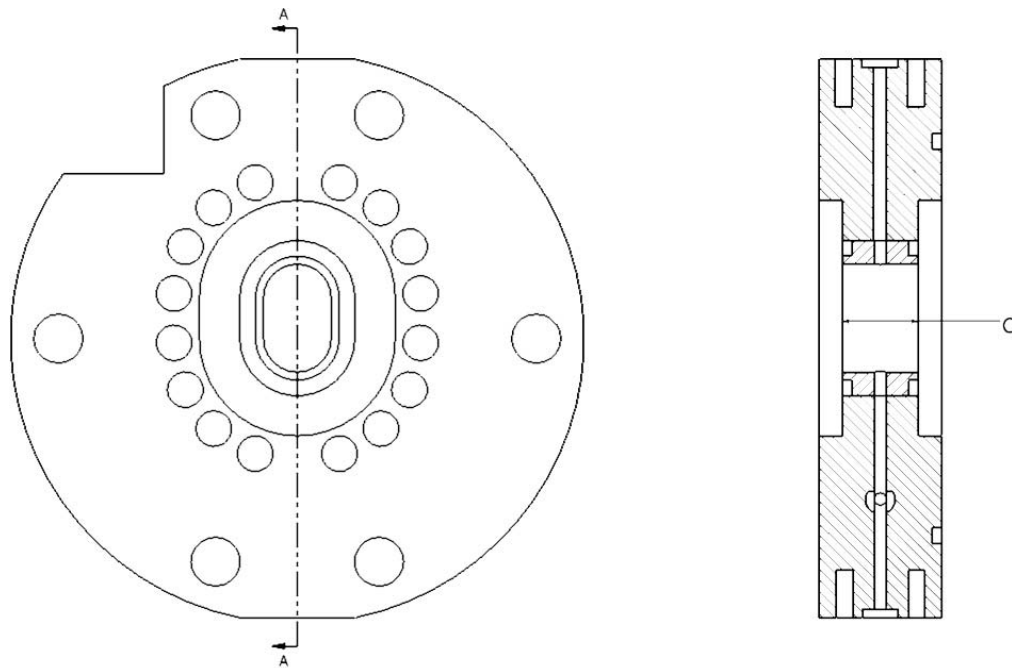
Figure 2-8: TS5 Center Flange Assembly Detail

Due to the original target thickness, the system was reaching a performance limit from penetration rather than insufficient heat transfer. This can be concluded due to the fact that the original 10 mm deep target was only range thick for void fractions of 0.06 and less. In order to evaluate the heat transfer performance of the system, it is necessary to be confident in the amount of beam on target. To resolve this design flaw the axial dimensions of the center flange were increased uniformly by 3 mm. This allows for the beam strike to lengthen (see dimension C in Figure 2-8) while still preserving the proper compression on the front and rear window foils. The redesigned flange was constructed solely of aluminum in order to reduce the fabrication cost. This allowed for a thermal analysis of the target, but due to the tendency of fluoride to react with aluminum this flange could not be used for production of fluoride ion.

Chapter 3

Target Instrumentation and Control

3.1 Control System Design

A PC-based data instrumentation and control system was developed to remotely operate the target and collect sensor data. The LabView software package and LabView Field Point hardware system were selected based on a combination of versatility, ease of implementation, adaptability, and low cost. This system is also portable, making it possible to transition from lab to production environments relatively quickly. The information flow in the system is illustrated figure 3-1.
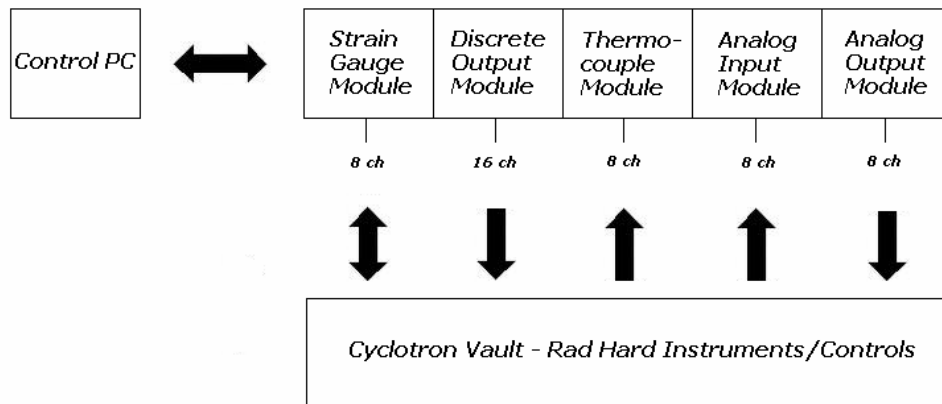
Figure 3-1: Field Point Hardware Hierarchy

Control PC – Runs the system software. Communicates with the Field Point Modules via RS-232 Protocol.

Strain Gauge Module – Provides both excitation and input for strain gauge type pressure transducers. Transducers of this type with no intrinsic signal conditioning perform better in high neutron fluence.

Discrete Output Module – Control finite state devices such as solenoid valves, single speed motors or pumps.

Analog Input Module – Interfaces with conventional loop current transducers and reads beam current reference signal.

3.2 Target Control

The target area in any accelerator becomes an extremely radioactive environment during and after a bombardment. Thus, it is critical to have a reliable system to remotely control the pumps and valves during the loading, beam on target, unloading, and rinsing phases of operation. Additionally, the thermosyphon target must be loaded and pressurized from the bottom of the beam strike, which requires more control valves and operating steps than a conventional reflux target system. This additional complexity makes the system well suited for automatic control. Figures 3-2 to 3-6 show the conceptual operation of the target control system.

The target chamber and expansion volume are initially sealed after being purged with helium. The loading reservoir is filled with target water.
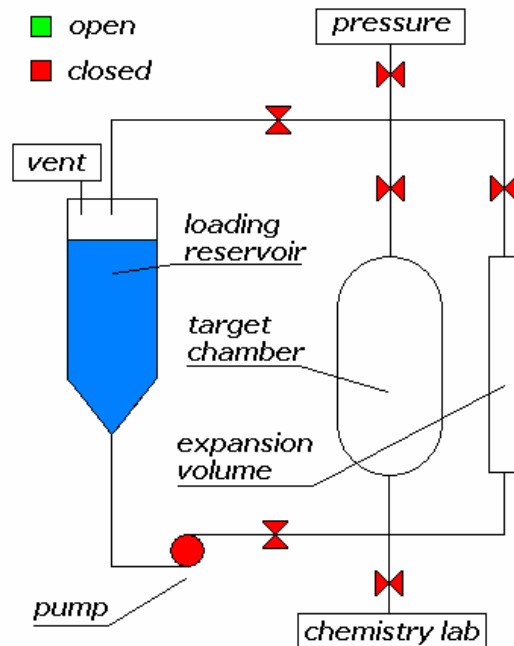
Figure 3-2: Target Operation State 1 of 5

Loading valves open and the loading pump begins to fill the target chamber. The path to the expansion volume is open, but the top valve is closed so very little fluid enters the expansion volume initially.
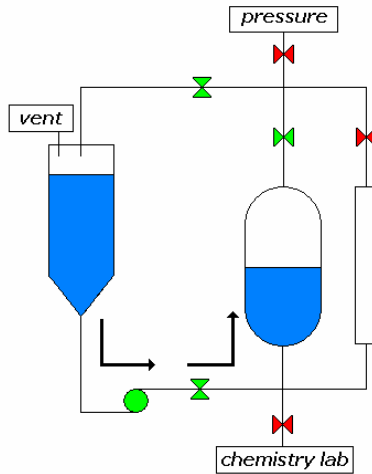
Figure 3-3: Target Operation State 2 of 5

After the target chamber fills completely, fluid returns to the loading reservoir and a circulating flow is established. The pressure at the bottom of the target chamber increases and pressurizes the gas in the expansion volume, allowing fluid to enter.
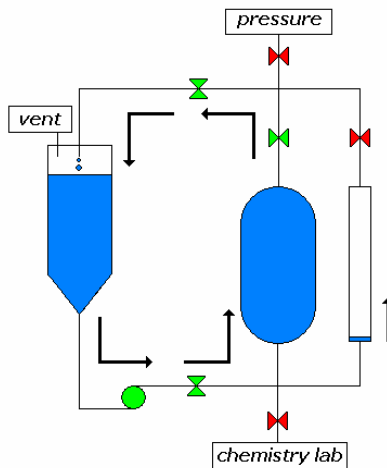
Figure 3-4: Target Operation State 3 of 5

Once the pressure in the expansion volume reaches equilibrium with the pressure generated by the circulating flow, the loading valves are closed and the expansion chamber is connected to a pressure source from above. The beam is then incident upon the target chamber for the duration of the bombardment.
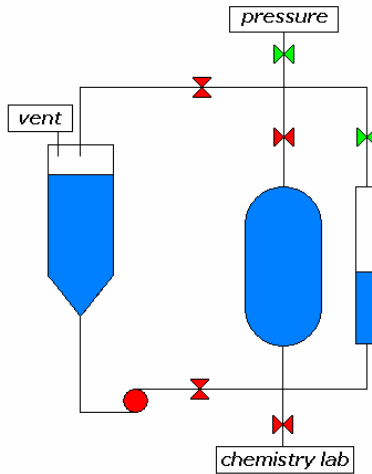
Figure 3-5: Target Operation State 4 of 5

When the bombardment is complete, the target chamber is evacuated by applying pressure from above. The irradiated water is delivered to a synthesis unit in the chemistry lab or simply to a dose calibrator. The water in the expansion chamber is evacuated afterwards, rinsing any residual activity from the delivery line.
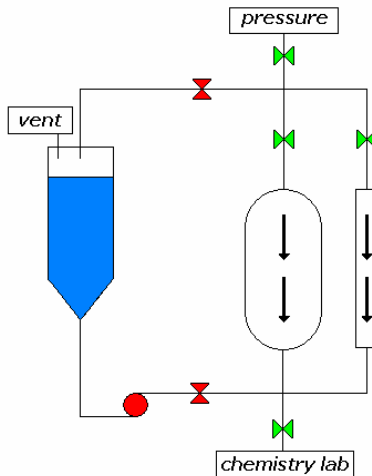
Figure 3-6: Target Operation State 5 of 5

18

Figure 3-7 shows the LabView target control screen. Each phase of system operation can be performed using automatic timed and interlocked sequences, which use sensor input to prevent undesirable operating conditions or control actions from occurring. Alternatively, the user can toggle control elements individually if special experiments or operating procedures are desired.
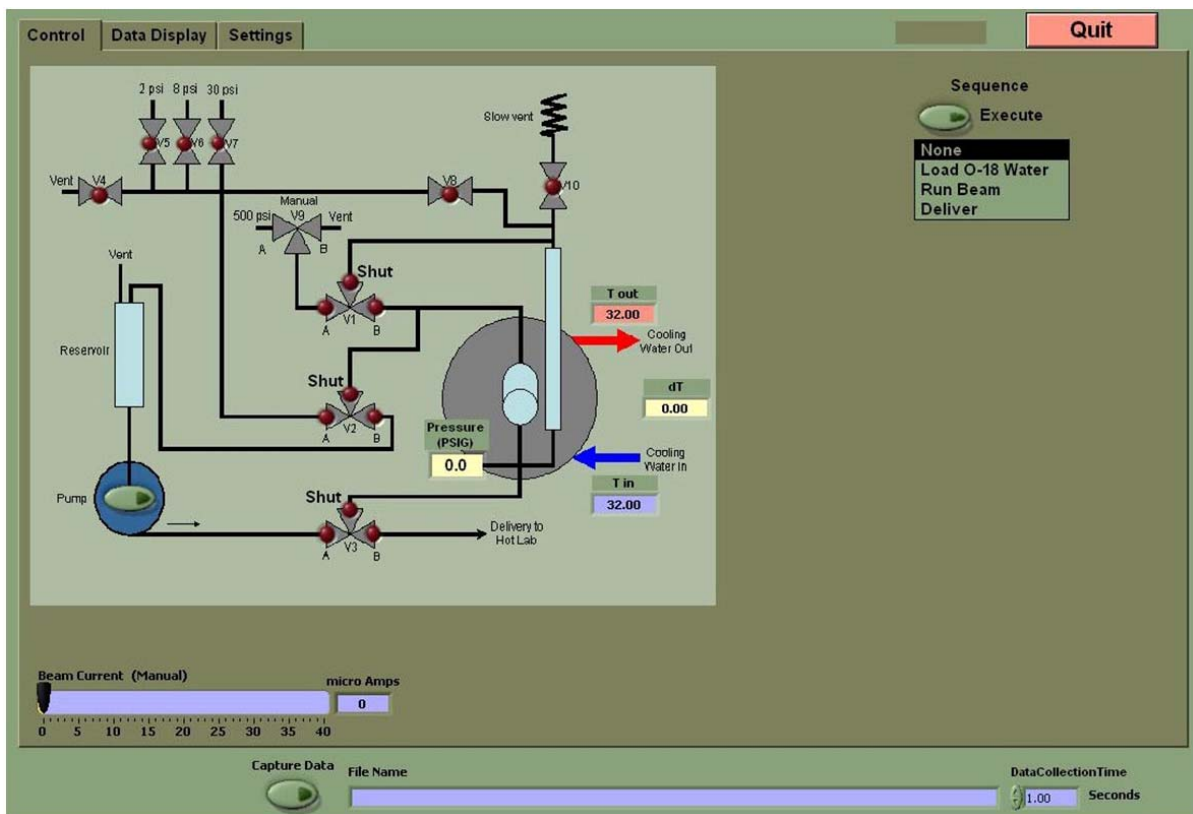
Figure 3-7: Target Control Software Interface

3.3 Data Acquisition

The target internal pressure, body temperature, and cooling water temperature are monitored and recorded to file. This allows the user to not only collect experimental data, but also to detect leaks and identify insufficient cooling or otherwise high temperature conditions. These signals are also used during the automated sequences as control interlocks. Figure 3-8 shows the data acquisition interface.
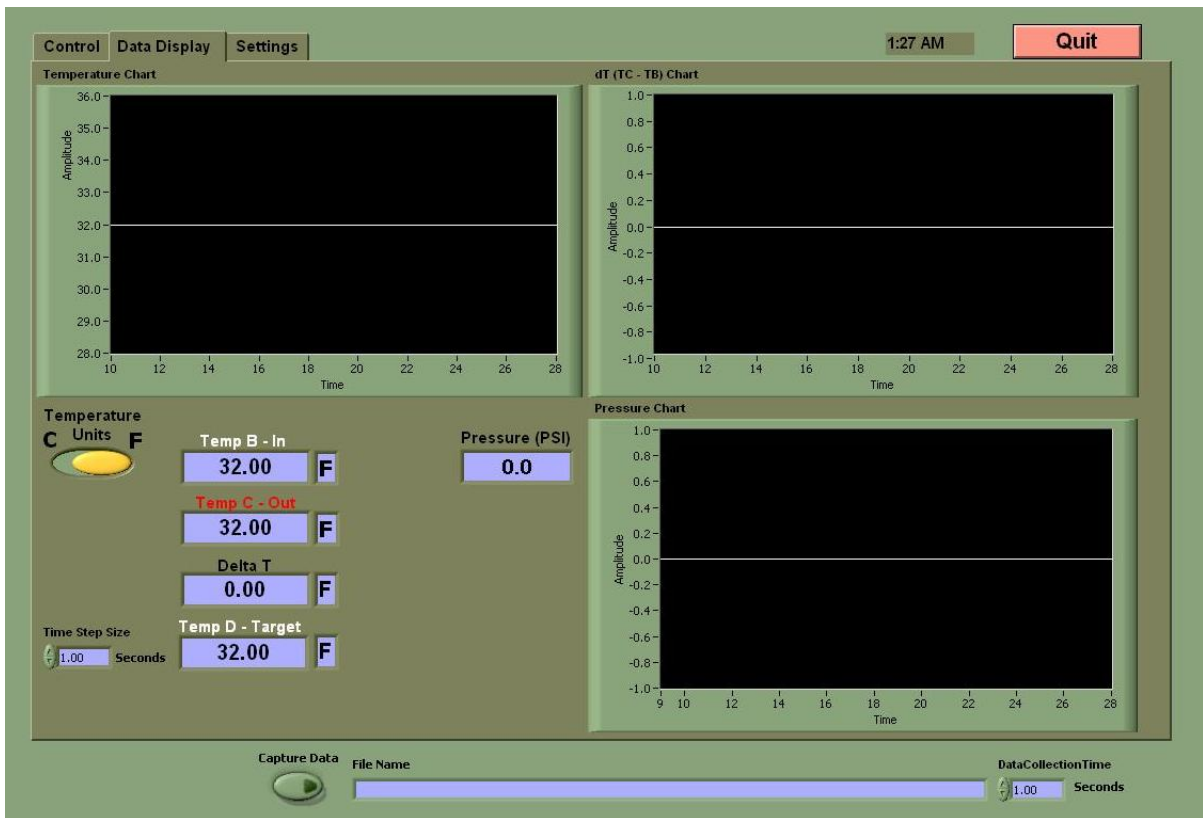
Figure 3-8: Data Acquisition Software Interface

Chapter 4

Experiments and Methods

4.1 Radiological Experiments and Calculations

The ultimate metric for target performance is the production capability of F-18 and, ultimately, ^{18}FDG. In order to achieve successful ^{18}FDG yields it is important to produce enough fluoride ion, albeit chemically reactive. It is possible to verify that the target is producing adequate F-18 by comparing experimental yields with theoretical yields. There are several methods to evaluate the chemical reactivity of the product, one being a decay corrected ratio of ^{18}FDG activity to initial F-18 activity. The following sections will discuss experiments for evaluating raw F-18 production as well as ^{18}FDG yield.

4.1.1 Experimental F-18 Yield Calculations

Both SRIM and the more general MCNPX were used to calculate the ratio of enriched water thick target yield (TTY) to 100% O-18 TTY from the $^{18}O(p,n)^{18}F$ nuclear reaction. For proton energies below 30 MeV, we find the calculated F-18 yields for enriched water to be reduced by no less than 25% of those for 100% O-18 [14]. We have also generated experimental TTY's from enriched water using a boiling water target that support the 25% figure.

The current majority of [F-18]radiosyntheses rely on [F-18]fluoride ion as starting material, produced from the $^{18}O(p,n)^{18}F$ nuclear reaction [12] on isotopically enriched [O-18]water. Experimental F-18 yields up to 30 MeV H+ have been reported; however, none of the target materials used were enriched water [5]. This report further suggests that F-18 yields derived from enriched water would be about 17% lower than for 100% enriched O-18.

Clearly the TTY will be lower for water, but it is not obvious by the amount stated. In an effort to effectively evaluate the performance of water targets for fluoride production, obtaining a validated correction factor can eliminate a significant amount of uncertainty.

The TTY for PET isotopes is defined as activity at saturation. The reaction rate can be derived from first principles and TTY can be calculated from the reaction cross section and stopping power.

Consider a collimated beam of protons with initial energy E_0 and intensity ϕ_0 incident upon an infinite homogeneous cylindrical volume of target material. The distribution of particles inside the target volume can be represented as

$$\phi(x, E') = \phi_0 \delta(E' - E(x)) \tag{1}$$

for all energies E' and beam energies E(x), given implicitly by the stopping power

$$E(x) = E_0 - \int_0^x \frac{dE}{dx'}\big(E(x')\big)dx' \tag{2}$$

This assumes that the energy-integrated intensity of particles does not have any spatial dependence, and is valid if the energy threshold of the reaction of interest is significantly higher than the Bragg energy.

The reaction rate inside the volume can be expressed as

$$R = A \int_0^\infty \int_0^\infty \phi(x, E') \Sigma(E') dE' dx \tag{3}$$

where A is the cross sectional area of the cylinder.

Substituting expression 1 yields

$$R = A\phi_0 \int_0^\infty \int_0^\infty \delta\left(E' - E(x)\right) \Sigma(E') dE' dx \tag{4}$$

$$R = A\phi_0 \int_0^\infty \Sigma\left(E(x)\right) dx \tag{5}$$

This can be expressed in more convenient parameters of beam current and effective length

$$R = I_{beam} \int_0^L \Sigma\left(E(x)\right) dx \tag{6}$$

The integral is evaluated numerically by the approximation

$$R = I_{beam} \sum_{n=1}^N \Sigma\left(E(x_{n-1})\right)(x_n - x_{n-1}) \tag{7}$$

The SRIM software package was used to generate stopping power tables for protons in pure ^{18}O and $H_2{}^{18}O$. Using these values to generate the spatial energy distribution and the published excitation function for the cross sections, TTY values were computed for proton energies up to 30 MeV.

As an alternate approach, the MCNPX code was also used to evaluate the effective reduction in yield. MCNPX is a general purpose Monte Carlo radiation transport code that is capable of simulating both neutral and charged particle transport in arbitrary geometries. When supplied with the excitation function, the code calculates the volumetric reaction rate directly.

Figure 4-1 and Table 4-1 show the results from both sets of calculations compared with published yields for 100% O-18. Both yield calculations and the published values show good agreement. The relative reduction in yield when comparing O-18 water to pure O-18 is

23

shown by the top set of curves. For proton energies of commercially available PET cyclotrons (8-30MeV), the reduction is between 24% and 26%.

Calculated F-18 Saturation Yields for Range Thick O-18 Enriched Gas and Water Targets
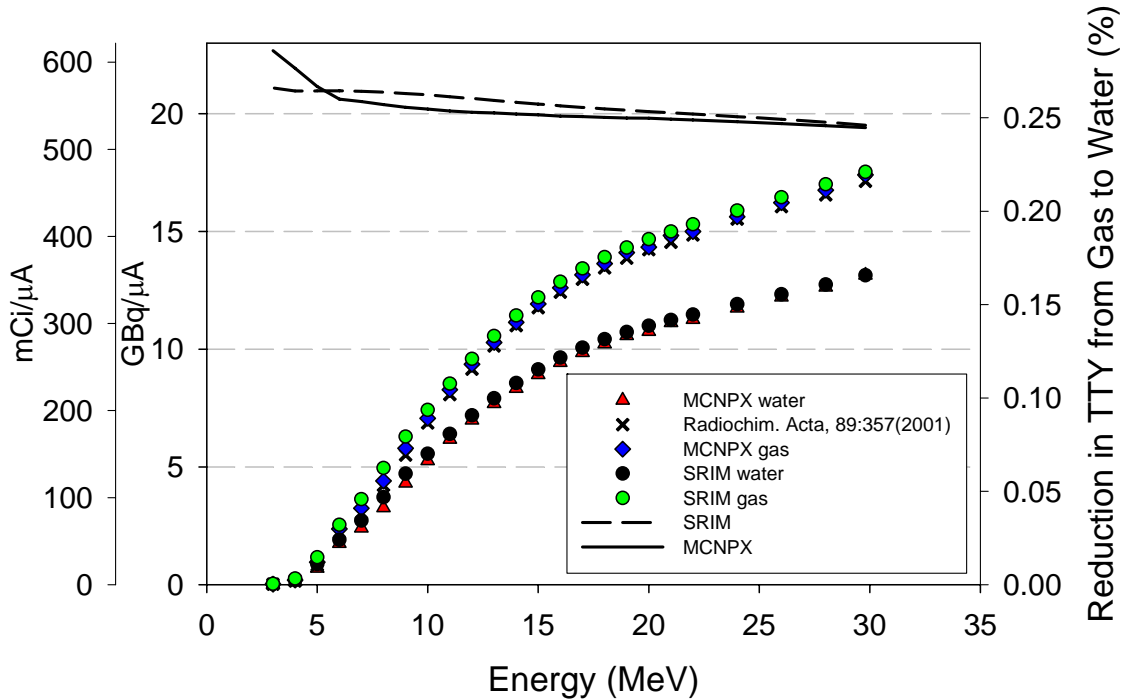
Figure 4-1: TTY calculated in SRIM and MCNPX

To verify the yields experimentally, TTY's were measured at the Duke University Medical Center (DUMC) using 97% enriched water in a silver thermosyphon target. The target depth was 13 mm, almost twice the range of a 27 MeV proton in water. After bombardment, the target was flushed and then rinsed twice to ensure most product ion had been collected. The activities were then measured in a Capintec (CRC-15 PET) dose calibrator, decay corrected to end of bombardment, and multiplied by the saturation factor.

Experimental results are included in Table 4-2. In addition to experiments performed at DUMC, experiments performed by Lepera and Strangis [7] support a reduction in yield of at least 25% from a water target.

Table 4-1: TTY calculated in SRIM and MCNPX

	MCNPX				SRIM				HESS
E	$H_2^{18}O$		$^{18}O_2$		$H_2^{18}O$		$^{18}O_2$		^{18}O
MeV	GBq/μA	mCi/μA	GBq/μA	mCi/μA	GBq/μA	mCi/μA	GBq/μA	mCi/μA	GBq/μA
5	0.7	18.9	1.0	25.8	0.9	23.2	1.2	31.5	0.8
6	1.8	47.3	2.4	64.0	1.9	50.7	2.6	68.9	2.2
7	2.4	65.1	3.3	87.8	2.7	72.2	3.6	98.1	3.0
8	3.3	88.4	4.4	119.0	3.7	98.7	5.0	134.0	4.2
9	4.3	116.5	5.8	156.6	4.6	125.3	6.3	170.0	5.5
10	5.3	142.3	7.1	190.9	5.5	148.0	7.4	200.6	6.9
11	6.2	167.1	8.3	223.9	6.3	170.5	8.5	230.9	8.1
12	7.0	189.0	9.4	253.1	7.1	191.8	9.6	259.3	9.2
13	7.7	207.9	10.3	278.1	7.8	211.4	10.6	285.4	10.1
14	8.3	225.3	11.1	301.2	8.5	229.2	11.4	309.0	11.0
15	8.9	241.2	11.9	322.3	9.1	244.9	12.2	329.7	11.8
16	9.4	255.2	12.6	340.7	9.6	258.5	12.9	347.6	12.4
17	9.9	266.5	13.2	355.7	10.0	270.2	13.4	362.9	13.0
18	10.2	276.4	13.6	368.7	10.4	280.1	13.9	375.8	13.5
19	10.6	285.9	14.1	381.2	10.7	288.6	14.3	386.9	13.9
20	10.8	290.7	14.3	387.4	11.0	296.1	14.7	396.6	14.2
21	11.1	300.9	14.8	400.7	11.2	302.9	15.0	405.4	14.6
22	11.3	304.5	15.0	405.3	11.5	309.4	15.3	413.6	14.9
24	11.8	317.6	15.6	422.2	11.9	321.8	15.9	429.4	15.5
26	12.2	330.2	16.2	438.4	12.4	333.8	16.5	444.6	16.1
28	12.6	341.5	16.8	452.9	12.8	345.7	17.0	459.5	16.6
30	13.1	355.2	17.4	470.3	13.2	357.2	17.5	473.8	17.1

Table 4-2: Experimental Thick Target Yields

Beam Current (μA)	Energy	TTY (mCi/μA)	% Theoretical	Source
5	27	313	0.7025	DUMC
20	27	332	0.7448	DUMC
20-35	19.4	275	0.710	[7]
10-20	24.2	291	0.6896	[7]

4.1.2 Experimental F-18 Physical Yields

The most important performance metric is the physical yield of $^{18}F^-$ from the water target. If the yield is lower than expected, there are generally two possible explanations. The most likely is that the beam is not stopping entirely in the target water. If protons are not slowing down in the target water, then the production reaction cannot occur and less fluoride activity will result. Another possibility is that the activity is being produced but is not completely recovered. It is for this reason that chemically inert materials are desirable.

Due to the high cost of ^{18}O enriched water, it is attractive to measure the experimental yields by bombarding natural abundance water. Oxygen-18 is present in natural water with an atomic fraction of 0.2%, so F-18 can still be easily detected and the results scaled accordingly. Unfortunately, using natural abundance water also results in the production of the short-lived isotopes ^{15}O (2 min) and ^{13}N (10 min), which must be allowed to decay before measuring the ^{18}F activity.

Once the activity of the target batch has been measured it must be corrected for decay back to the activity present at end of bombardment (EOB).

$$A(t_{EOB}) = \frac{A(t)}{e^{-\lambda(t-t_{EOB})}} \tag{8}$$

λ is the radioactive decay constant defined as

$$\lambda = \frac{\ln(2)}{T_{1/2}} \tag{9}$$

The ^{18}F activity at EOB must then be corrected by a saturation factor to determine the experimental saturation yield. The saturation factor can be derived from the traditional

ordinary differential equation for production and decay, with initial condition $N_F(0)=0$.

$$\frac{dN_F}{dt} = \Sigma_O \phi - \lambda N_F(t) \tag{10}$$

Applying an integrating factor yields

$$\frac{d}{dt} N_F(t)e^{\lambda t} = \Sigma_O \phi e^{\lambda t} \tag{11}$$

Integrating 11 gives the analytical solution

$$N_F(t) = \frac{\Sigma_O \phi}{\lambda}(1-e^{-\lambda t}) = N_F(\infty)(1-e^{-\lambda t}) \tag{12}$$

This can be rearranged to define the saturation factor

$$\frac{N_F(t)}{N_F(\infty)} = 1 - e^{-\lambda t} \tag{13}$$

Since it would take an extremely long time to effectively reach saturation for F-18, the saturation factor can be used for correcting activity from short bombardments to expected activity at saturation conditions. Combining these expressions and dividing by beam current gives the saturation yield as a function of experimentally measured activity.

$$\frac{A_{sat}}{I_{beam}} = \frac{A(t)}{I_{beam}e^{-\lambda(t-t_{EOB})}(1-e^{-\lambda(t_{EOB}-t_{BOB})})} \tag{14}$$

The thick target saturation yield is most often expressed in units of mCi/μA or GBq/μA and is strictly a function of proton energy.

Table 4-3 contains experimental yields from the 10 mm thick TS5 target using natural water. It is clear that the target produced a lower than acceptable amount of F-18 at any beam current. At a beam current of 20μA, the yield dropped dramatically, indicating that the

performance has been further compromised. This corresponded to an increase in boiling oscillations that can be seen in the thermal hydraulic experiments. Boiling oscillations are indicative of instability produced by beam penetration. Beam penetration would decrease proton fluence on target material and lead to a diminished yield.

Table 4-3: Experimental TTY from TS5
26 MeV/400 psig/10 mm/ 0.001" Havar/Natural H_2O

I_{beam} (μA)	Experimental (mCi/μA)	Projected (mCi/μA)	Yield Ratio
5	213	332	0.64
10	208	332	0.63
17	220	332	0.66
20	121	332	0.36

Though it was clear that the target was not performing as anticipated, there was still a desire to determine the production capabilities of the design. To this end, F-18 yields were measured at lower energies. After two bombardments, it was decided that, due to such low yields, it was not cost effective to continue or to perform [18]FDG syntheses. Yields from the enriched water runs are included in Table 4-4.

Table 4-4: Experimental TTY from TS5
22 MeV/400 psig/10 mm/0.001" Havar/Enriched H_2O

I_{beam} (μA)	Experimental (mCi/μA)	Projected (mCi/μA)	Yield Ratio
5	209	300	0.69
20	102	300	0.34

In the course of measuring natural abundance water yields, it became apparent that a significant fraction of ^{13}N produced was volatile and escaping the target during

depressurization. This was confirmed by capturing a 1000 mL sample of purge gas from the target delivery line and analyzing it via radio-gas chromatography (SRI6610C with Carrol-Ramsey 1055 radiation detector). The traces from the mass and activity analyses show peaks for nitrogen, indicating that the activity in the sample was likely $^{13}N_2$ (Figure 4-2).
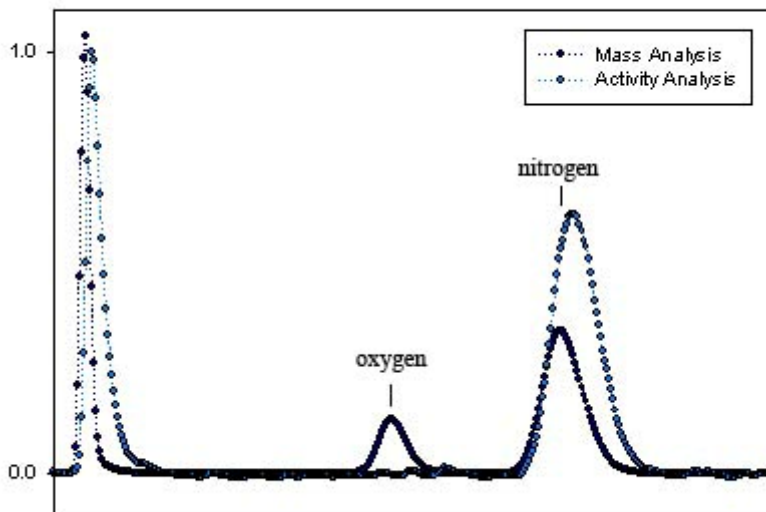
Figure 4-2: Gas Chromatograph Analysis of Target Purge Gas

The presence of radio-labeled nitrogen gas has implications for the experimental data as well as for the standard operating procedures for these types of experiments. If a significant amount of volatile activity is produced, then it must be trapped and allowed to safely decay. In addition, there did not appear to be a consistent ratio of volatile activity to aqueous activity, so the activity in the target water from ^{13}N was not a reliable indication of beam fluence on target.

The production of $^{13}NH_4^+$ is quite common in PET centers with on-site accelerators. The preferred production method is via the $^{16}O(p,\alpha)^{13}N$ reaction, in which natural abundance water plus 1-10 ppm ethanol is used as the target material [16]. The volatile activity is

mitigated by the addition of the ethanol. The presence of any organic compounds, even in very low concentrations can result in poor fluoride recovery and ^{18}FDG synthesis. Hence, ethanol is never used in F-18 water targets.

For the purposes of our experiments, however, it was a priority to gain a better quantitative estimate of beam fluence on target. Since the target was not performing adequately for production use, contamination was not of great concern. By using low concentrations of ethanol in the target water and measuring the ^{13}N activity, faster measurements can be made and the wetted target surface material becomes much less critical.

Due to the high cost of tantalum fabrication, the second target flange was constructed of aluminum. Yield tests were conducted for ^{13}N to estimate fluence on the target material. The results from these experiments are included in Table 4-5. The ratio of actual to expected yield shows dramatic improvement when compared to the initial target design. In order to use this design for F-18 production, however, a new center flange of sufficient depth would need to be fabricated with a tantalum liner.

Table 4-5: Experimental ^{13}N TTY from TS5
22 MeV/400 psig/10 mm/0.001" Havar//10 ppm ETOH

I_{beam} (µA)	Experimental (mCi/µA)	Projected (mCi/µA)	Yield Ratio
5	38.8	41.0	0.95
10	39.8	41.0	0.97
10	41.6	41.0	1.02
15	38.3	41.0	0.94
20	34.1	41.0	0.83
20	39.1	41.0	0.95
25	35.4	41.0	0.86
25	33.1	41.0	0.81

4.2 Thermal Hydraulic Experiments

4.2.1 Sight Tube Experiments

The most extensive thermal hydraulic testing of the TS5 target system was performed using a glass sight tube attached between the expansion chamber and vent valve. The sight tube has an internal diameter of 3 mm which corresponds to approximately 70 µL of volumetric expansion per 10 mm level rise. The target was then filled until water became visible in the sight tube, pressurized, and subjected to beam. This method provides two key pieces of information about the target operation. Primarily, it can be used to identify the operating regions of the target system. In addition, it is possible to quantify the amount of vapor present in the target based upon level changes in the sight tube.

The regions of operation can be observed by inspecting the sight tube level as a function of beam current. At relatively low beam intensities, there is sufficient heat rejection by the target in the absence of boiling and the level in the sight tube rises linearly with beam intensity from thermal expansion. As the bulk fluid temperature in the target approaches saturation (boiling, not isotopic saturation), there is a small amount of subcooled boiling. This is likely due to bubble formation on the window foil or local bubble formation in the beam. This small amount of boiling causes no detectable level change in the sight tube but rather a vibration in the meniscus which can be noted. As the heat input is increased further, the level in the sight tube begins to oscillate slowly (approximately 2-3 times per second).

Figures 4-2 and 4-3 correspond to sight tube data for the 10 mm and 13 mm TS5 targets, respectively. Both were operated at a beam energy of 22 MeV and pressure of 400 psig. In both target configurations, the onset of boiling occurs at a slightly lower beam current than did the corresponding reduction in yield from the previous section. It is likely

that the power range of operation between the onset of boiling and beam penetration due to voiding can be quite narrow [8,9]. Figure 4-4 illustrates this behavior. This would be especially true of a target with high conduction resistance like the TS5. As a result, it is not unexpected that the physical yield diminishes shortly after boiling initiation.
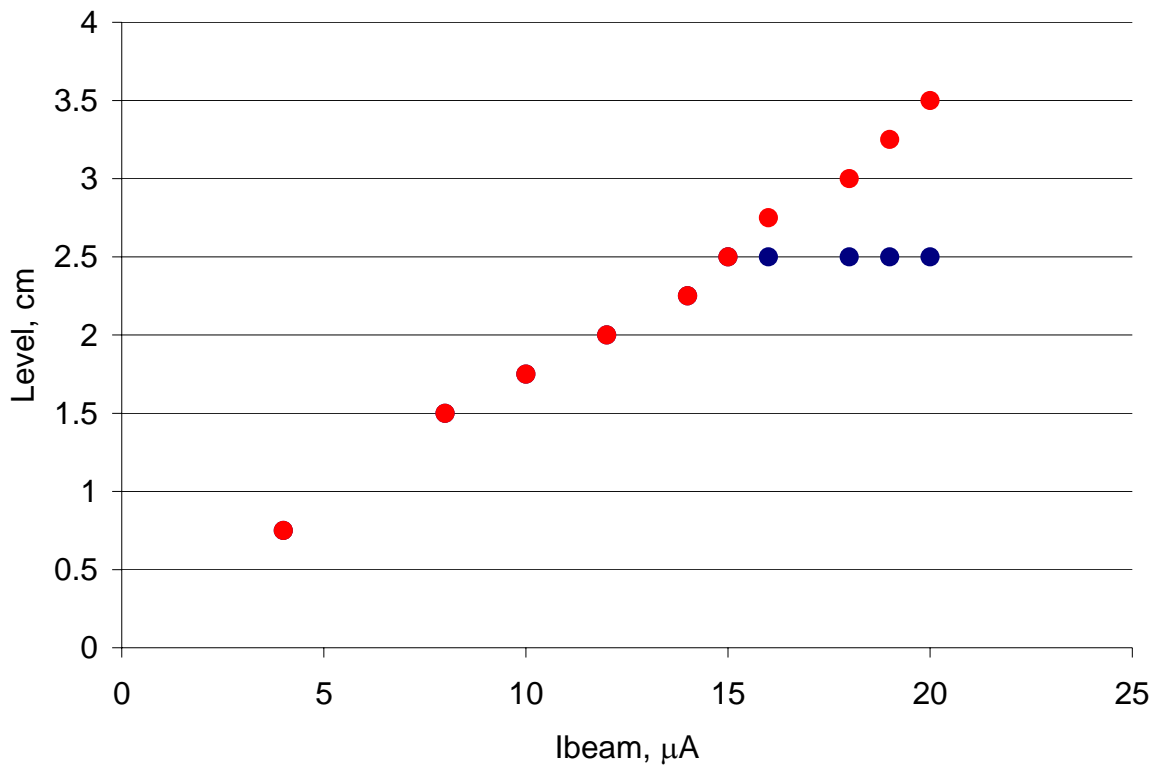

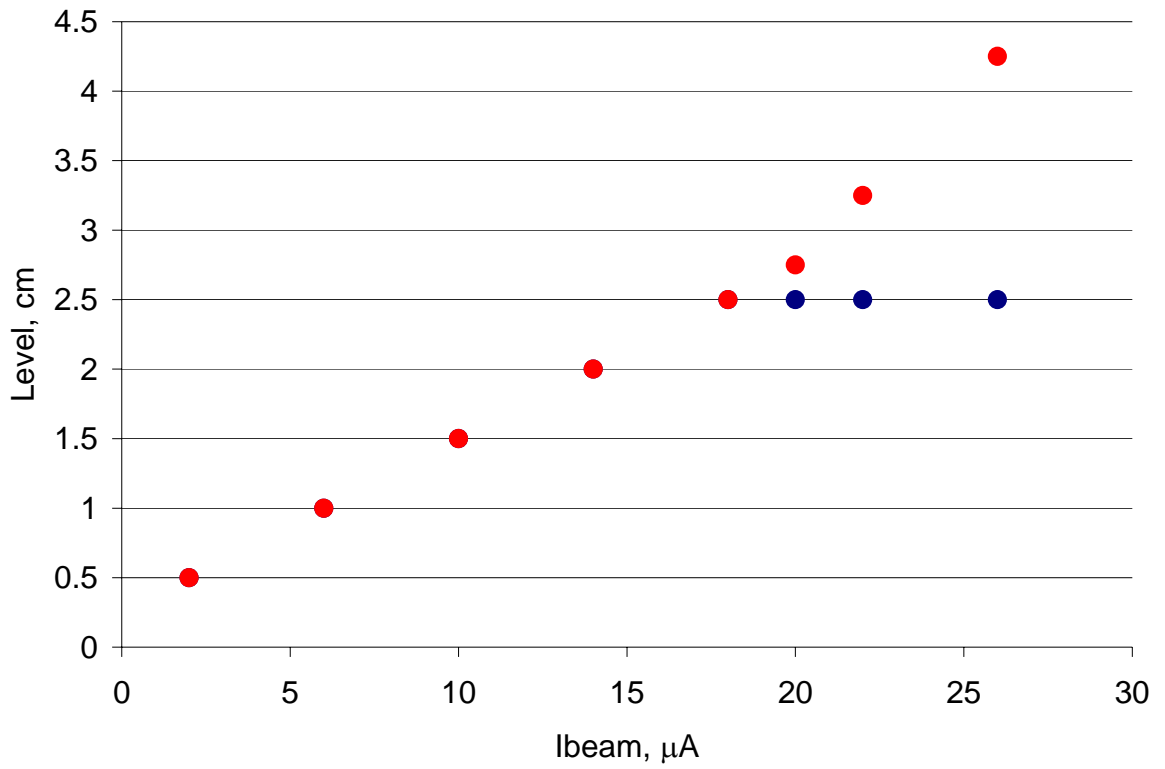**Figure 4-3: Sight Tube Level as a Function of Beam Current (10 mm Deep Target)**

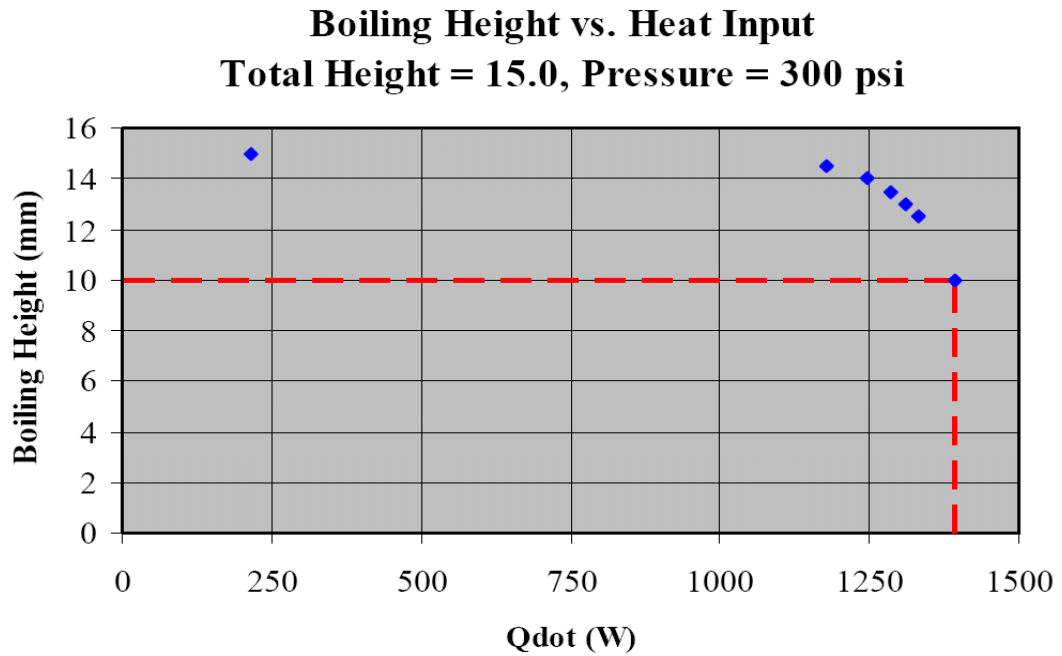**Figure 4-4: Sight Tube Level as a Function of Beam Current (13 mm Deep Target)**

Figure 4-5: Boiling Level vs. Heat Input for TS6 (Peeples 2006)

4.2.2 Target and Cooling Header Flow Measurements

Pressure versus flow measurements were taken for both the chilled water header supplying the cyclotron and the TS5 target itself. This data is primarily used to determine the heat removal from the target by the chilled water. Since the chilled water system at the Duke facility is tied into many hospital systems, the pressure fluctuates and constant flow cannot be assumed. Additionally, the characterization of the chilled water header will benefit future target designs.

Table 4-6 contains flow and pressure data for the chilled water header. This set of measurements was taken by short circuiting the high and low pressure headers across a gate valve and ERDCO mechanical flowmeter (P/N 4165K111). The pressure losses in the headers become evident at high flowrates but should not be of concern as these values are far in excess of what is needed to cool targets at even multi-kilowatt power levels.

Table 4-6: Pressure versus Flow of Chilled Water Header

flow rate, GPM	flow rate, cm^3/sec	P_{supply}, psig	P_{return}, psig
0	0	87	0
0.5	32.2	87	2
1.0	63.6	86	2
1.5	95.3	86	3
2.0	126	85	4
2.5	158	85	6
3.0	189	85	7
3.5	221	85	8
4.0	252	84	9
4.5	284	84	10
5.0	316	84	11
5.5	347	84	13

Tables 4-7 and 4-8 contain flow and pressure data for the TS5 target with the two different rear window designs and the 10 mm tantalum center flange. This data can be used to generate an online heat removal figure based on inlet and exit temperatures and pressures in the control system:

$$\dot{Q} = \dot{m} C_p \left(t_{out} - t_{in} \right) = f \left\{ P_{in} - P_{out} \right\} C_p \left(t_{out} - t_{in} \right) \tag{15}$$

Also, if convective heat transfer coefficients are to be approximated for use in numerical models, the flow rates must be measured.

Table 4-7: Differential Pressure versus Flow for TS5 with Grid Rear Window

flow rate, GPM	flow rate, cm^3/sec	ΔP, psid	ΔP, kPa
0.5	30	5	34
0.7	41	8	55
0.8	50	10	69
1.3	79	25	172
1.5	97	40	276
1.7	108	53	365
1.9	122	60	414
2.1	133	75	517

Table 4-8: Differential Pressure versus Flow for TS5 with Solid Rear Window

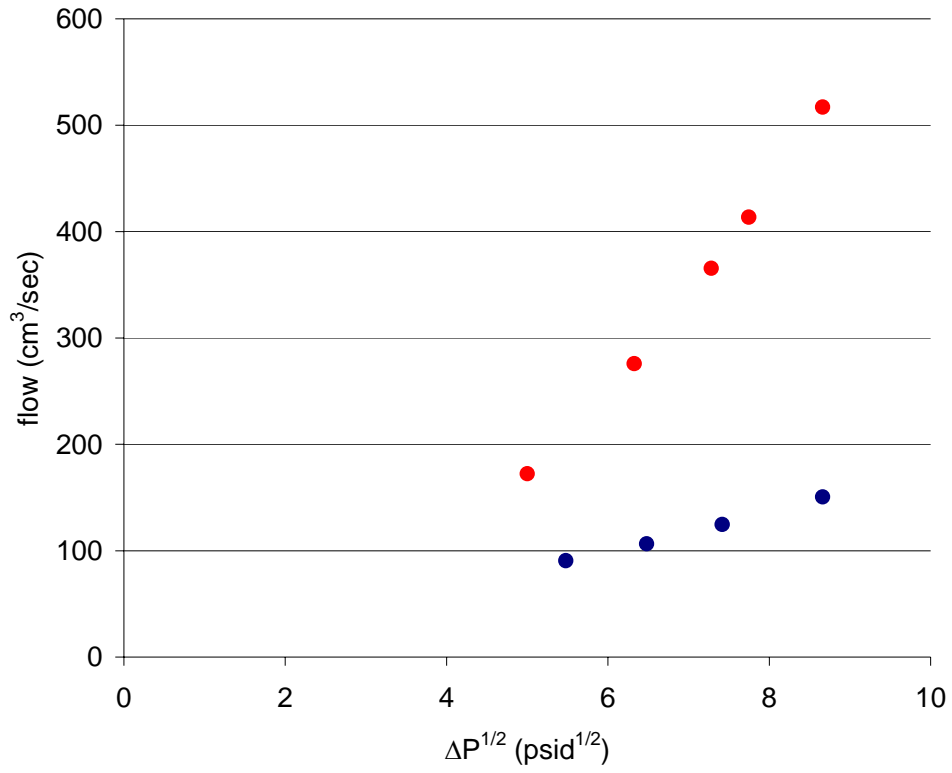| flow rate, GPM	flow rate, cm^3/sec	ΔP, psid	ΔP, kPa
0.5	30	5	34
0.6	41	8	55
0.8	51	10	69
1.4	91	30	207
1.7	106	42	290
2.0	125	55	379
2.4	151	75	517
2.6	163	80	552

Figure 4-6: Differential Pressure versus Flow for TS5

4.2.3 Target Internal Heat Distribution

Identifying the regions of thermal resistance between the target chamber and cooling channels is paramount to increasing the heat rejection capabilities of the system. The internal temperature distribution was measured during target operation at different power levels. This was done by drilling holes in the center flange of the 13 mm aluminum target at several axial and radial positions. Measurements included both the boiling and condensing regions. Thermocouples were then inserted and bonded to the surface with a silver based compound to ensure good thermal contact.

This experiment provides a clear map of heat flow in the target body. Figure 4-6 shows the instrument locations and values obtained in the experiment. The most significant observation is that the condensing region has a much higher heat flux than the boiling region. This is expected due to the larger heat transfer coefficient in the condensing region. In addition, the rear of the flange is hotter than the front. This is likely the result of axial conduction within the target structure. The cooling water enters the target as a jet on the rear window, and then enters an annular plenum where it turns and flows into radial cooling channels (see Figure 1-1). The radial cooling channels extend beyond the target chamber into an exit plenum in the front of the target. There is a much shorter axial conduction path from the target chamber to the front plenum than to the rear plenum.

When compared with 2-D simulation results from COMSOL, the trends are very similar. However, the simulation results predict much higher than observed temperatures in all areas of the target body. Figure 4-7 shows the 2-D COMSOL model of TS5. The most likely explanation for this discrepancy is that there exists a significant amount of axial conduction within the structure of the target that cannot be captured in this two dimensional
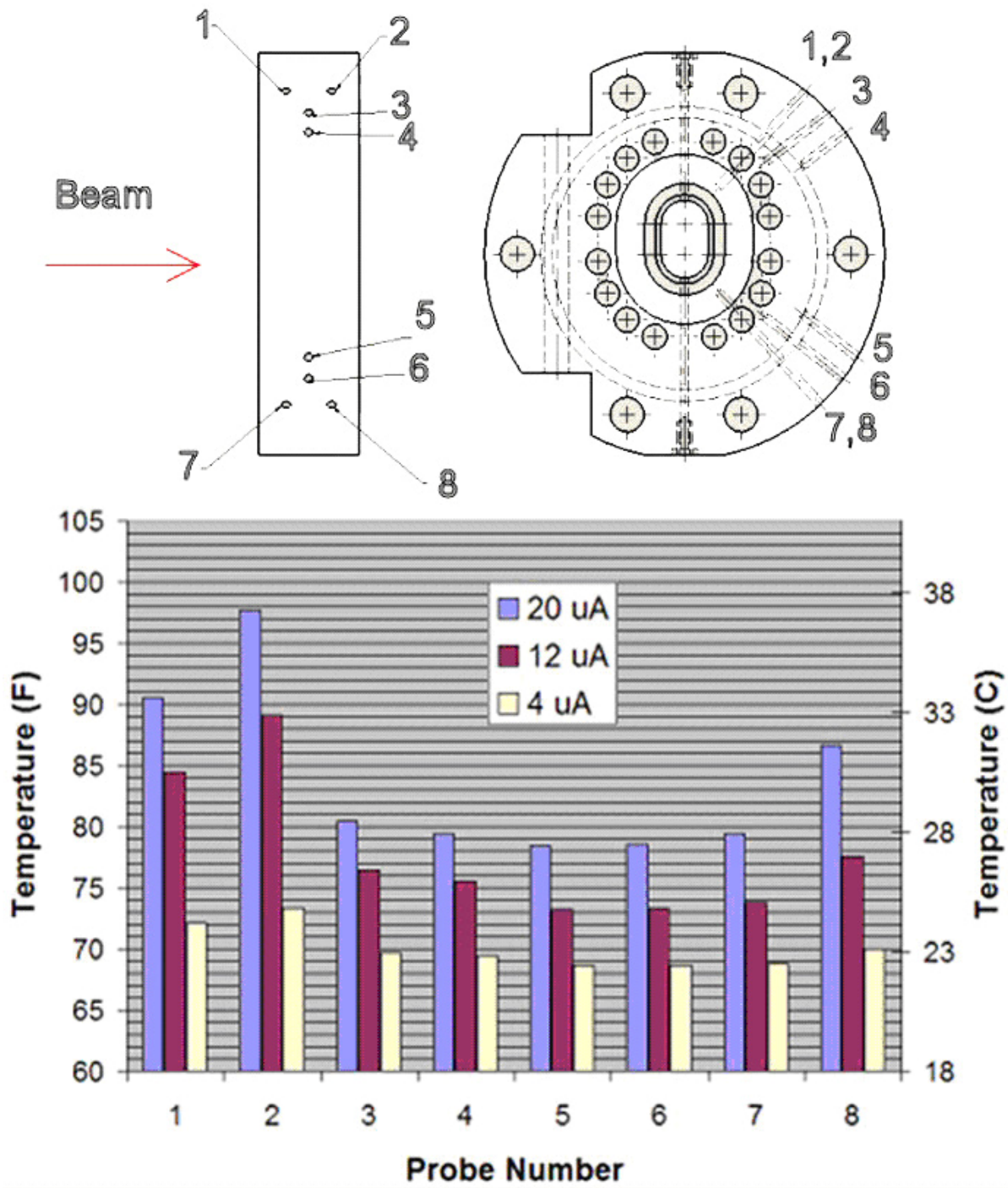
Figure 4-7: Experimental Temperature Distribution Measurement

model. The effective surface area of each cooling channel is much greater since it extends beyond the region of symmetry that the 2-D model represents. There is no way to experimentally verify this with the TS5 since the target is cooled in a single pass and there is no isolation between the axial and radial cooling water. Finally, the model does not account for heat loss through the back foil. Future modeling efforts can be improved by allowing for these phenomena.
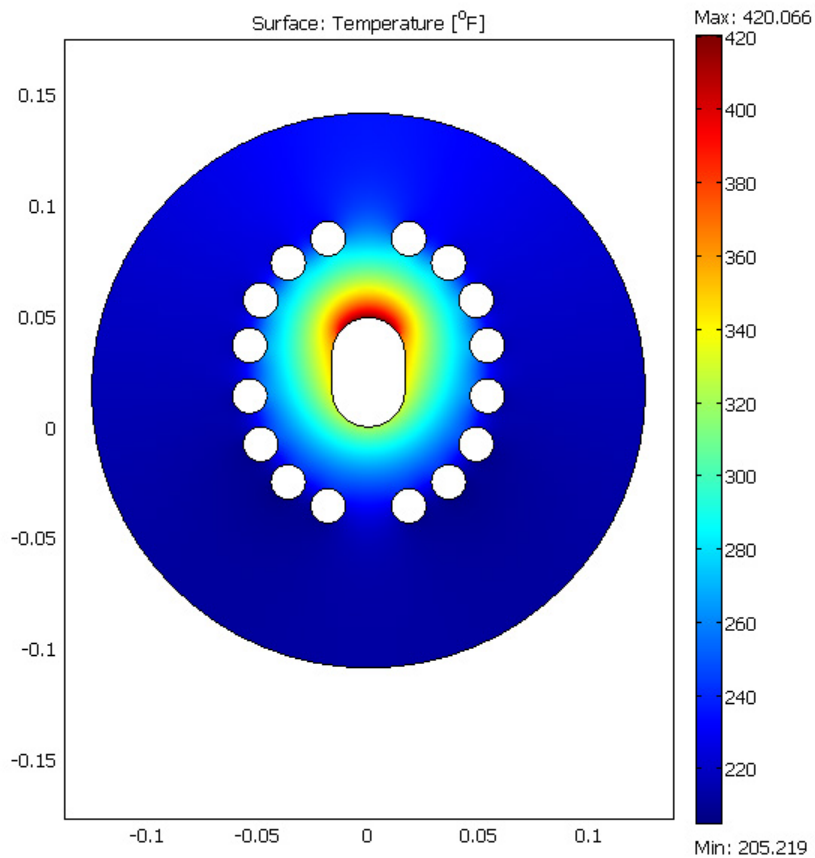

Figure 4-8: COMSOL Two Dimensional Model of TS5 (Peeples 2006)

Chapter 5

Conclusions

5.1 Summary and Conclusions

The analysis of the TS5 thermosyphon target included thermal hydraulic and radiochemical experiments as well as computational modeling. The target was not well suited for routine production on the CS-30 accelerator at Duke University Medical Center. However, a great deal of information was learned about the behavior of bottom-pressurized boiling water proton targets. A comprehensive characterization procedure was developed and will be implemented in future target designs.

5.2 Application of Findings to Future Targets

A next generation thermosyphon, creatively named TS6, has been designed and is currently in fabrication. Figure 5-1 shows a solid model of the target. Insight from the characterization of TS5 has proven invaluable to both the mechanical design and computational analysis of this new target.

The most significant design aspect of the TS6 is the monolithic core, which integrates both the target chamber and cooling passages into a solid piece of tantalum. This is made possible by incorporating an exit plenum for the radial cooling channels before they reach the front window. In the TS5, the wall-to-hole spacing was dictated by the front window foil o-ring groove. With the new design, the radial cooling passages can be in very close proximity to the chamber wall, thus reducing the conduction thickness considerably. In addition, the modeling is much simplified by removing the tantalum/aluminum interface between the cooling channels and chamber wall.
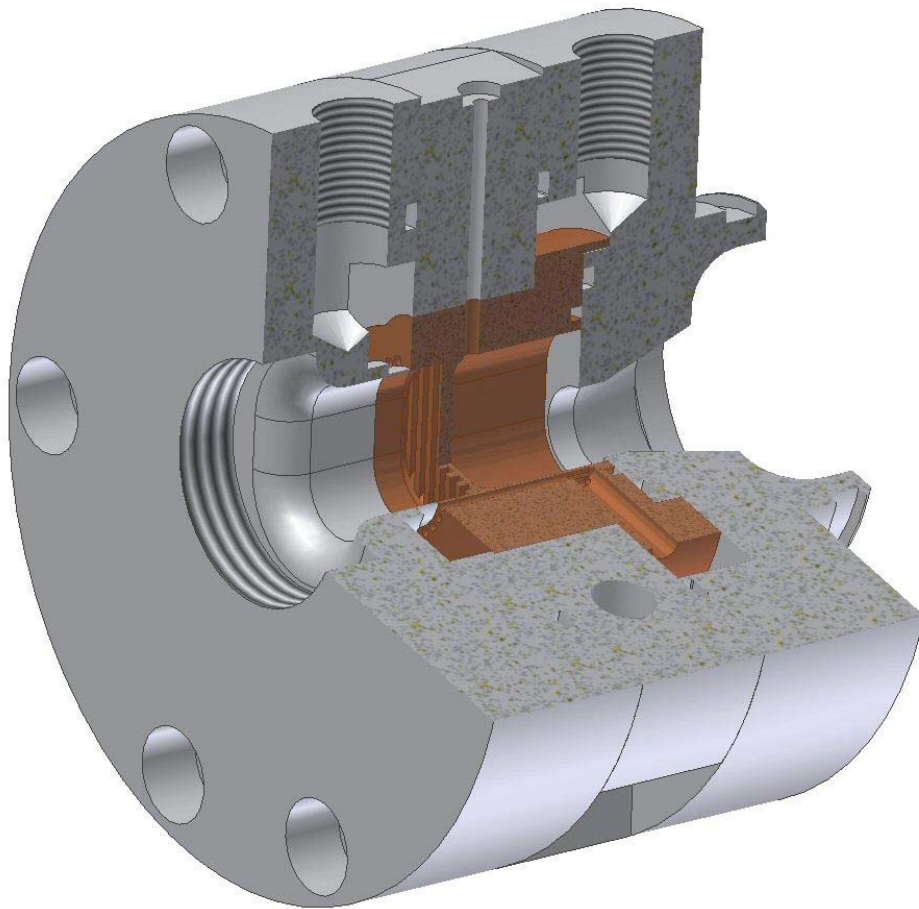
Figure 5-1: TS6 Assembled Solid Model (Humphrey 2006)

Another improvement is the isolation of radial channel and rear window cooling loops. The immediate benefit is increased flow velocities in both systems by placing them in parallel rather than in series. Just as importantly, however, measuring the heat removal of the cooling loops independently provides valuable information. The ratio of rear window cooling to radial channel cooling would increase in the event of beam penetration, providing a detection mechanism for that event. Additionally, the computational models can be better calibrated to the experimental data if the measurements are independent.

5.3 Future Work

Next generation TS target systems will likely be marketed for installation in new isotope distribution centers as well as for retrofit in existing centers. Customers will not only be interested in increased heat rejection capability, but also in system reliability and product chemical quality. In order to meet these needs, it is important to anticipate new complications not only from the complexity necessary to operate a target of this type, but also from running at high energies, beam currents, power levels, and fluences.

A more evolved instrumentation and control system will be implemented. In addition to the capabilities of the current system, additional signals will be measured and data will be logged for reliability and failure modes analyses. In addition to measuring beam current, beam shape will be measured in real time. This will be done initially by installing a four segment ring collimator, but ultimately the hope is that high resolution 2-D intensity maps can be generated in real-time at operating power levels. System components, especially those in close proximity to the beam strike, will likely experience a shortened life-span, so radiation hard materials and devices will be needed.

Equally important to the operating power level of the system is the chemical quality of the fluoride ion produced. Clearly, there is no advantage to running the accelerator at a higher power level and producing larger batches of product ion if the net amount of ^{18}FDG activity produced is not increased. In order to identify contaminants introduced by running at high power levels, several radiochemical analyses will be performed including neutron activation analysis of water samples at the NCSU Pulstar Reactor. These techniques can also be used to identify the onset of critical heat flux in the window foil, a potentially serious failure mechanism at high beam currents.

Finally, more robust computational models are needed to accurately map the flow of thermal energy inside the target. Three-dimensional conduction models will be implemented in COMSOL as well as ANSYS CFX. These conduction models will ultimately be coupled with convective heat transfer and fluid flow models to accurately simulate the heat removal by the cooling water. In the beam strike, a radiation transport code, most likely MCNPX, will need to be coupled to a multiphase computational fluid dynamics (CFD) simulation. This will present a unique set of challenges as multiphase fluid dynamics is primarily an empirical field, and multiphase CFD is still in its infancy. A small number of commercially available packages does exist; however, the applicability to this specific research is uncertain.

References

1. Clark J.C. High-Powered Cyclotron Recirculating Targets for Production of the ^{18}F Radionuclide. North Carolina State University. Raleigh, North Carolina: 2004.

2. COMSOL Multiphysics Version 2.3, COMSOL Inc., Sweden, 2006.

3. Doster J.M., Roberts A., and Wieland B.W. "New Cyclotron Targetry to Enhance F-18 PET," *Trans. Amer. Nuc. Soc.* 88: 269, 2003

4. Doster J.M., Clark J., and Wieland B.W. "Recirculating Targetry to Enhance F-18 Clinical PET," *Trans. Amer. Nuc. Soc.* 91: 841, (2004)

5. Hess E., Takàcs S., Scholten B., Tàrkànyi F., Coenen H. H., and Qaim S. M. Excitation function of the ^{18}O(p,n)^{18}F nuclear reaction from threshold up to 30 MeV. *Radiochimica Acta*. 89:357–362, 2001.

6. MCNPX Monte Carlo N-Particle eXtended 2.6C, LA-UR-06-7991, 2006.

7. Lepera C. G., Strangis, S. R. "Thick Target Yields for the Reaction ^{18}O(p,n)^{18}F above 16 MeV." *AIP Conference Proceedings* 576: 313-314, 2001.

8. Peeples J.L. Design and Optomization of Thermosyphon Batch Targets for Production of ^{18}F. Master of Science Thesis, North Carolina State University. Raleigh, North Carolina: 2005.

9. Peeples J.L., Humphrey M.S., Doster J.M., and Wieland B.W. "Finite Element Modeling of Thermosyphon Batch Targets," *Proceedings of the Eleventh Workshop on Targetry and Target Chemistry*. Cambridge, UK: 2006.

10. Phelps M.E. PET: Molecular Imaging and Its Biological Applications. New York: Springer-Verlag, 2004.

11. Armstrong I.S., Barnhart T.E., Roberts A.D. "Modeling the Optimal Design of a Grid Support System and Observations of Relevant Contaminants for PETTrace High Yield ^{18}F-Fluoride," *Proceedings of the Eleventh Workshop on Targetry and Target Chemistry*. Cambridge, UK: 2006.

12. See Satyamurthy N., Amerasekera B., Alvord C.W., Barrio J.R., and Phelps M.E. Tantalum [^{18}O]Water Target for the Production of [^{18}F]Fluoride with High Reactivity for the Preparation of 2-Deoxy-2-[^{18}F]Fluoro-D-Glucose. *Molecular Imaging and Biology*. 4:65-70, 2002. and references cited therein.

13. Stokely M., Bida G., Humphrey M.S., Doster J. M., and Wieland B.W. "High Yield Thermosyphon Targets for Production of ^{18}F-Fluoride," *Proceedings of the Eleventh Workshop on Targetry and Target Chemistry*. Cambridge, UK: 2006.

14. Stokely M., Bida G., Doster J. M., and Wieland B.W. "Correction Factor to Obtain Thick Target Yields for $H_2^{18}O(p,n)^{18}F$ from $^{18}O(p,n)^{18}F$," *Proceedings of the Eleventh Workshop on Targetry and Target Chemistry*. Cambridge, UK: 2006.

15. Valk P.E., Bailey D.L., Townsend D.W. and Maisey M.N. Positron Emission Tomography: Basic Science and Clinical Practice. New York: Springer-Verlag, 2003.

16. Wieland B.W., Bida G., Padgett H., Hendry G., Zippi E., Kabalka G., Morelle J., Verbruggen R, and Ghyoot M. In-target Production of [^{13}N] Ammonia via Proton Irradiation of Dilute Aqueous Ethanol and Acetic Acid Mixtures. *Applied Radiation and Isotopes*. 42:1095-1098, 1991.

17. Wieland B.W., Wright B.C., Bida G.T., Illan C.D., Doster J.M., Clark J.C., and Runkle R.C. "Thermosyphon Batch and Regenerative Turbine Recirculating $^{18}O(p,n)^{18}F$ Water Targets for Operation at High Beam Power," *Proceedings of the Tenth Workshop on Targetry and Target Chemistry*. Madison, WI: 2004.

18. Ziegler J.F. SRIM 2003 The Stopping and Range of Ions in Matter, SRIM, 2006.